Supporting Information

Vertically aligned hematite nanosheets with (110) facets controllably exposed for ammonia synthesis with high faraday efficiency beyond 2.5 A cm^{-2}

Jinfeng Liu,†[a] Shiwen Du,†[b] Wenjun Fan,[a] Qinglin Li,[a] Qi Yang,[a] Lin Luo,[a] Jiangnan Li[a] and Fuxiang Zhang*[a]

a. State Key Laboratory of Catalysis, Dalian Institute of Chemical Physics, Chinese Academy of Sciences, Dalian National Laboratory for Clean Energy, Dalian 116023, Liaoning, China.

b. School of Physics and Materials Engineering, Dalian Minzu University, Dalian 116600, China.

Experimental Procedures

Materials and Chemicals.

Potassium hydroxide (KOH, ≥ 99.0%), iron nitrate nonahydrate ($Fe(NO_3)_3 \cdot 9H_2O$, ACS grade), potassium nitrate (KNO_3, 99%), potassium nitrite (KNO_2, 99.99%), ethanol (≥ 99.5%), Nafion aqueous solution (5.0 wt.%), ammonium chloride (NH_4Cl, 99.99%), sodium hypochlorite solution (NaClO), hydrochloric acid (HCl 36 wt%), Carbon paper was used as a substrate which was cleaned by ultrasonic assisted washing with isopropanol/ethanol/DI water step by step before utilization.

Preparation of the Fe_2O_3 nanosheets arrays electrocatalysts

Fe_2O_3 nanosheets (denoted as Fe_2O_3-NS) arrays electrocatalysts were synthesized by one in-situ electrochemical reconstruction on its Fe_2O_3 nanorods (denoted as Fe_2O_3-NR) which was synthesized through typical hydrothermal method and subsequent by a simple calcination. In detail, 1 mmol of $Fe(NO_3)_3 \cdot 9H_2O$ and 1 mmol of Na_2SO_4 were added in 30 mL of H_2O under the ultrasonic until to form a transparent solution. Then a pretreated carbon cloth (2 × 3 cm^2) and the mixed solution were transferred into a Teflon-lined autoclave, which was sealed and kept at a constant temperature of 120 °C for 6 h. After that, the resultant samples were fully rinsed with water and dried overnight under vacuum. Finally, the red brown Fe_2O_3 catalyst was obtained by annealing the precursor at 400 °C for 2 h with a heating rate of 1 °C min^{-1} under a nitrogen atmosphere. Subsequently, the samples were activated in 1 M KOH and 0.1 M KNO_3 by a continuous 20 cycles CV sweeping at a rate of 50 mV s^{-1} from 0 to -0.5 V vs. RHE for the structural reconstruction. The electrocatalyst mass loading of Fe_2O_3-NS was ca. 0.6 mg cm^{-2}.

The synthesis of Fe_2O_3 NP electrocatalyst

For comparison, the Fe_2O_3 nanoparticles were prepared by the calcination of $Fe(NO_3)_3$ under a constant temperature of 400 ℃ for 2h in atmosphere with a heating rate of 1 °C min^{-1}. The resulted sample was regarded as Fe_2O_3-NP.

Characterization

Powder X-ray diffraction patterns were performed on a SmartLab X-ray powder diffractometer with Cu Kα radiation (λ=0.154178 nm). Scanning electron microscopy (SEM) images were taken by JSM-7900F. A Hitachi HT7700 was used for low-resolution TEM images, and a JEM 2100 was used to take the HRTEM images. XPS measurements were taken by a Thermo ESCALAB 250Xi with monochromatized Al Kα source (15 kV, 10.8 mA). The calibration of binding energies obtained in the XPS spectral analysis were performed by referencing C 1s to 284.8 eV.

XAS measurement

XAS experiments were carried by the 1W1B beamline of Beijing Synchrotron Radiation Facility (BSRF). The in-situ electrochemistry XAS data were measured in a solution mixed with 1 M KOH and 0.1 M KNO_3 in a homemade electrochemical cell which contains a catalyst-coated graphene paper, Hg/HgO (filled with 1 M KOH solution) electrode, and a Pt wire as the working electrode, reference electrode counter electrode, respectively. In-situ XAS measurements were carried in fluorescence mode by a Lytle detector and the corresponding reference samples were collected in transmission mode. All the electrochemical measurements were carried on a CHI 760E workstation. The acquired XAFS data were processed according to the standard procedures using the ATHENA module of Demeter software packages.

Electrochemical Measurements

All the performances of nitrate electroreduction were performed on a Gamry electrochemical workstation in a H-type cell separated by Nafion 117 membrane under room temperature and pressure. A three-electrode configuration contains a Hg/HgO (filled with 1 M KOH solution) as the electrode reference a, a platinum foil as counter electrode and a working electrode were used for nitrate reduction measurements. The surface of working electrode was 0.118 cm^2. For electrocatalytic NO_3^- reduction, 40 mL of electrolyte solution contain 1M KOH and 0.1M KNO_3 was used as the cathode

and anode compartment, respectively. The electrolyte was purged with high-purity Ar for 20 min before the measurement to remove the dissolved oxygen. The LSV curves were performed at a rate of 10 mV s^{-1}. The potentiostatic tests were carried in the constant potentials for 20 min at a constant stirring rate. High-purity Ar was continuously fed into the cathodic compartment during the experiments. The stability experiments of electrocatalytic reduction of nitrate to ammonia was conducted in a self-made continuous flow H-cell with a three-electrode system (Figure S12). Two reagent bottles filled with 10 L of electrolyte solution are connected to the cathode and anode, respectively. The anode is filled with a 1 M KOH solution, and the cathode is filled with a mixture containing 1 M KOH and 0.1 M KNO_3. The corresponding electrolyte solutions for the cathode and anode are circulated through a flow pump at a rate of 10 mL per minute. All measured potentials were calculated with respect to the RHE by the following equation:

$$E_{RHE} = E_{Hg/HgO} + 0.0591 * pH + 0.098 - 0.9 * i * R_s \qquad (1)$$

where i is the current and R_s regards as the solution resistance determined by electrochemical impedance spectroscopy (EIS).

Electrochemical active surface area (EASA) measurements were tested on a CHI 760E potentiostat. The cyclic voltammetry curves were taken in open circuit potential around ±50 mV at the different scan rates in a mixed solution of 1M KOH and 0.1 M KNO_3 purified with high-purity Ar. The plot of current density at set potential against scan rate has a linear relationship and its slope is the C_{dl}. The specific capacitance of a flat surface was assumed as 60 μF cm^{-2}.

$$S_{ECSA} = \frac{C_{dl}}{60\ \mu F\ cm^{-2}}$$

Electrochemical impedance spectroscopy (EIS) was carried out at a Solartron electrochemical workstation at -0.35 V versus RHE with a frequency range of 0.01 - 10^6 Hz for each catalyst in the mixed solution containing 1M KOH and 0.1 M KNO_3.

In-situ FTIR measurement

In-situ Fourier Transform Infrared Spectroscopy (FTIR) with attenuated total reflection (ATR) configuration was employed to study the adsorption of intermediates during the electroreduction of nitrate to ammonia. Surface Enhanced Infrared Absorption Spectroscopy (SEIRAS) tests were conducted using a full-band high-resolution infrared spectrometer (SHIMADZU IRTracer-100). The working electrode was prepared by uniformly drop-casting the catalysts onto a hemicylindrical silicon prism coated with a thin film of gold. A Pt wire and a Hg/HgO electrode served as the counter and reference electrodes, respectively. Before the test, argon (Ar) was continuously bubbled into the electrolyte including 1M KOH and 0.1M KNO_3 to remove dissolved O_2. The incident angle of the IR beam on the reflection plane of the electrode was approximately 60^o. The spectra resolution is 16 cm^{-1} for all measurements. The electrochemical data were recorded on the CHI760E working station with a three-electrode system.

Determination and quantitation of NH_3

The produced NH_3 was determined by the indophenol blue method. Detailly, the target electrolyte solution (2 mL) was moved into a clean vessel. Sequentially, adding 2 mL of 1M NaOH solution containing 5 wt% salicylic acid and 5 wt% sodium citrate, followed by the addition of 1 mL of 0.05 M NaClO and 200 uL of 1.0 wt% sodium nitroferricyanide ($C_5FeN_6Na_2O$) solution. After 2h in dark at room temperature, the absorption spectrum was measured by using a UV-vis spectrophotometer (UV-2600). The absorbance wavelength of 655 nm was chosen to determine the formation of indophenol blue. To accurately quantify the produced NH_3, concentration-absorbance standard curve was established by a series of standard ammonia chloride in 1M KOH and 0.1M KNO_3 solutions.

Determination and quantitation of nitrite

The produced NO_2^- was determined by the Griess test. 1 g p-aminobenzenesulfonamide was disperse in 100 mL of 3 M HCl solution (marked solution A). Then, 0.1 g N-(1-Naphthyl)ethylenediamine dihydrochloride was dissolve

in 100 mL ultrapure water as the color reagent (marked solution B). Sequentially, 1mL solution A and B are added in the target electrolyte solution (2 mL). The absorption intensity at a wavelength of 540nm was recorded after 10 min. The concentration-absorbance curves were calibrated using a series of standard KNO_2 in the solution of 1 M KOH and 0.1 M KNO_3.

Calculation of the faradaic efficiency and yield rate of NH_3.

The faradaic efficiency (FE) of electrocatalytic NO_3^-conversion was calculated as follows:

$$FE_{NH_3} = (8 \times F \times C_{NH_3} \times V)/(17 \times Q)$$

$$FE_{NO_2^-} = (8 \times F \times C_{NO_2^-} \times V)/(46 \times Q)$$

The yield rate of NH_3 was calculated using the following equation:

$$Y_{NH_3} = (C_{NH_3} \times V)/(t \times S)$$

where F is the Faraday constant (96,485 C mol^{-1}), C_{NH3} is the measured NH_3 concentration, V is the volume of the cathodic electrolyte, Q is the total charge passing the electrode, t is the reduction time, and S is the surface area of working electrode.

For H_2 products, the Faradaic efficiency (FE) was measured as follows:

$$FE_{H_2}(\%) = \frac{i_{H_2}}{i_{total}} \times 100\% = X_{H_2} \times f \times N_A \times \frac{F}{i_{total}} \times 100\% \quad (2)$$

Where i_{H2} represent as the partial current of H_2, i_{total} is the total current, f is the Ar flow rate (mol s^{-1}), N_A is the number of exchanged electrons to produce species g from H_2, and the F is Faraday constant (96485 C mol^{-1}).

^{15}N isotope-labeling experiment

An isotope-labeling experiment using mixed solution of 1 M KOH and 40 mM $K^{15}NO_3$ (98 atom% ^{15}N) as the electrolyte was carried out by 1H nuclear magnetic resonance (NMR, 400 MHz) to clarify the source of NH_3. The D-H_2O as a solvent and maleic acid ($C_4H_4O_4$) as the internal standard. 400 μL of the electrolyte solution was

mixed with 100 uL D-H_2O (with 0.04 wt% $C_4H_4O_4$). After $^{15}NO_3^-$ electroreduction at −0.35 V (vs. RHE), the obtained $^{15}NH_4^+$ was test. $^{14}NH_4^+$ was obtained at the same process as that of $^{15}NH_4^+$ except that the $K^{15}NO_3$ was replaced by $K^{14}NO_3$

The half-cell energy efficiency for producing NH_3

The half-cell energy efficiency (EE) was defined as the ratio of fuel energy to applied electrical power, which was calculated with the following equation:

$$E.E.(NH_3) = \frac{(1.23 - E^0_{NH_3}) \times F.E.(NH_3)}{1.23 - E} \times 100\%$$

Where E^0_{NH3} is the standard electrode potential (0.69 V) of nitrate electroreduction to ammonia in alkaline media, FE(NH_3) is the faradaic efficiency for NH_3; 1.23 V is the equilibrium potential of water oxidation (assuming the overpotential of the water oxidation is zero); E is the applied potential for the production of NH_3.

Calculation details

Density functional theory (DFT) calculations were conducted using the Vienna Ab Initio Simulation Package (VASP). The method of the Perdew-Burke-Ernzerh (PBE) of generalized gradient approximation (GGA) functional was utilized to describe the electronic exchange-correlation potential. DFT+U method was used to account for the Fe 3d electrons with the effective Hubbard U value of 4.3 eV according to the previous report. The periodic slabs with three layers of (110) and (104) crystal faces for Fe_2O_3 were built to evaluate their surface reactions. Meanwhile, a vacuum layer of 15 Å is applied for all the calculated slab models. The kinetic-energy cutoff was set as 500 eV to ensure all atoms except the bottom layer were fully relaxed for each system. The Monkhorst-Pack meshes of 2 × 3 × 1 and 1 × 2 × 1 were used in Brillouin zone sampling for the (110) and (104) slabs, respectively. Energy and force will not reach convergence until lower to 1.0×10^{-5} eV and 0.015 eV/Å, respectively. The adsorption energy ΔE of molecule A on the substrate surface is defined as

$$\Delta E = E_{*A} - (E_* + E_A)$$

where E_{*A}, E_A, and E_* denote the energies of surface-adsorbed molecule A, free molecule A, and the bare substrate, respectively.

The Gibbs free energy change (ΔG) for each elementary step as follows:

$$\Delta G = \Delta E + \Delta E_{ZPE} - T\Delta S$$

where ΔE is the adsorption energy, ΔE_{ZPE} is the zero-point energy difference and ΔS is the entropy difference between the gas phase and adsorbed state.

Assembly of the Zn-NO_3^- battery

The Fe_2O_3-NS and Zn plate were employed as the cathode and anode for Zn-NO_3^- battery, respectively. A typical H-type cell that contains 40 mL cathode electrolyte (1 M NaOH + 0.1M NO_3^-) and 40 mL anode electrolyte (5 M NaOH) separated by a bipolar membrane. The discharging polarization curves with a scan rate of 5 mV s^{-1} and galvanostatic tests were conducted using CHI 760E workstation at room temperature, respectively. After electrochemical test, the electrolyte was diluted to a certain concentration for the next products detection. The power density (P) of Zn-NO_3^- battery was determined by P = I ×V, where I and V are the discharge current density and voltage, respectively. The electrochemical reactions in Zn-NO_3^- battery were presented as following:

Cathode reaction: $NO_3^- + 7H_2O + 8e^- \rightarrow NH_4OH + 9OH^-$

Anode reaction: $4Zn + 8OH^- \rightarrow 4ZnO + 4H_2O + 8e^-$

Overall reaction: $4Zn + NO_3^- + 3H_2O \rightarrow 4ZnO + NH_4OH + OH^-$

Supplementary Figures and Tables

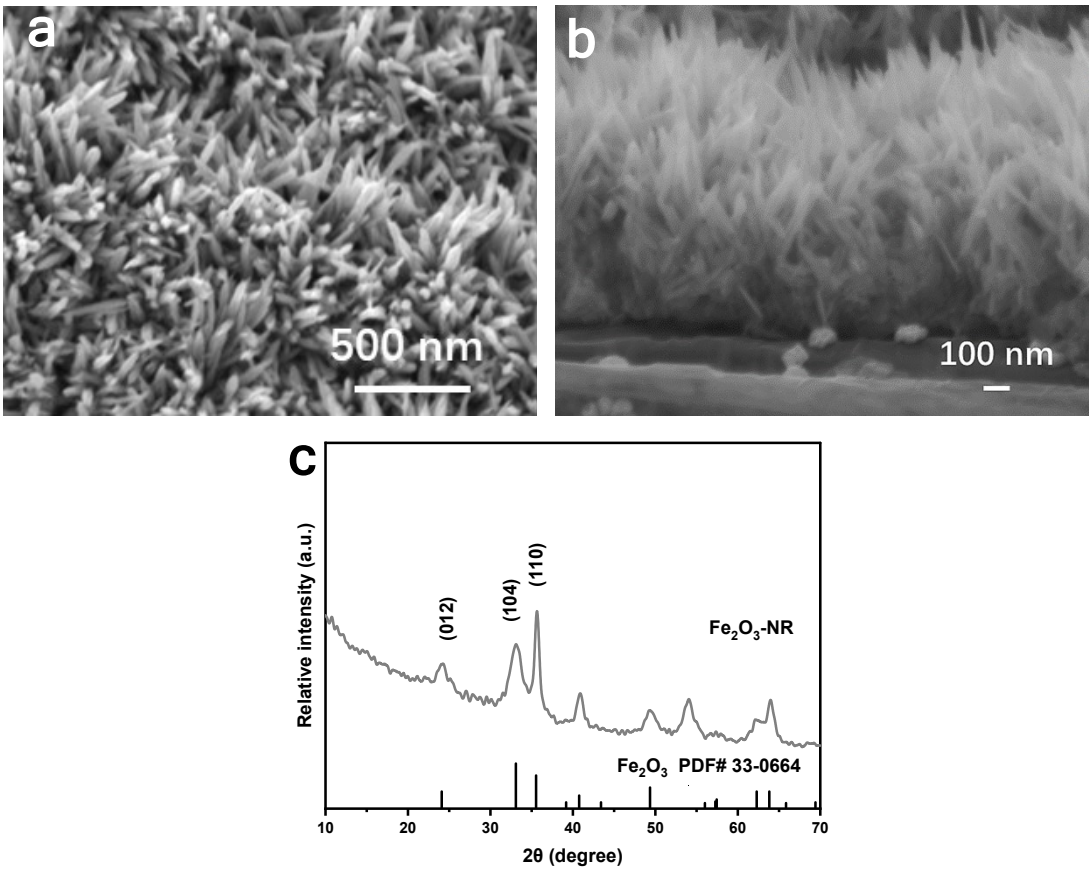

Figure S1. Structural characterizations of Fe_2O_3-NR: (a, b) SEM image and (c) XRD pattern.

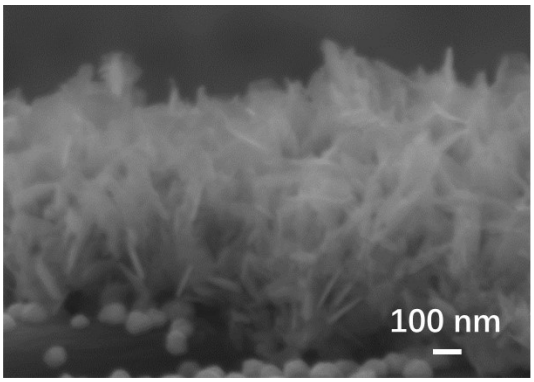

Figure S2. The SEM image of cross-sectional view of Fe_2O_3-NS.

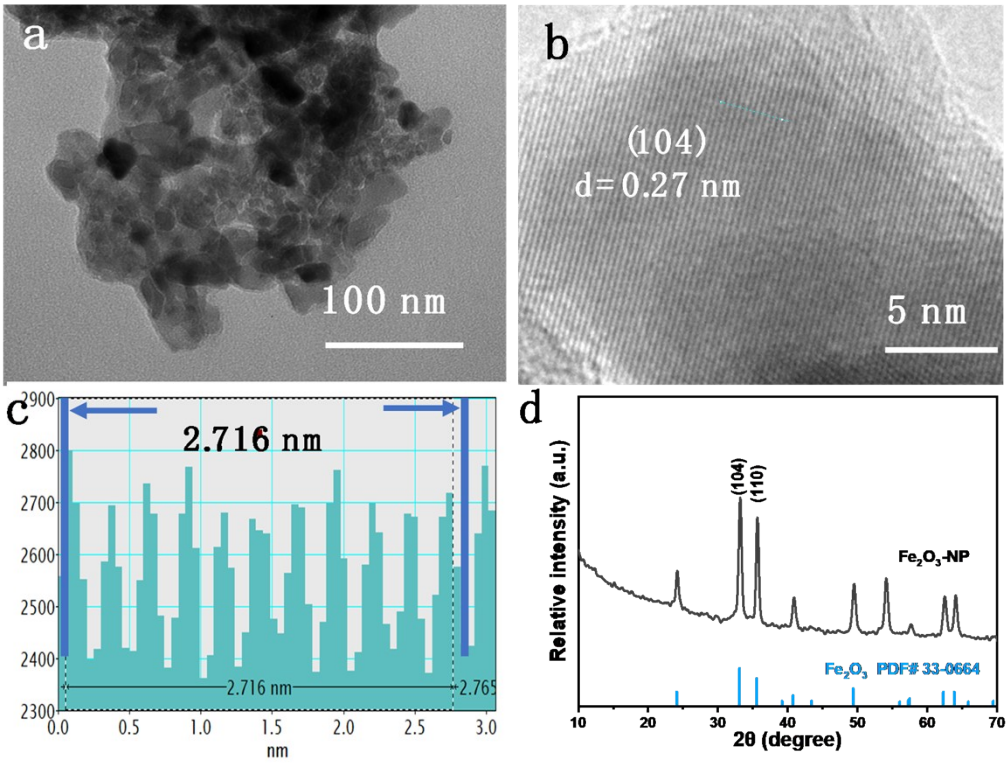

Figure S3. Structural characterizations of Fe_2O_3-NP catalyst: (a) TEM image, (b, c) high resolution TEM, and (d) XRD pattern.

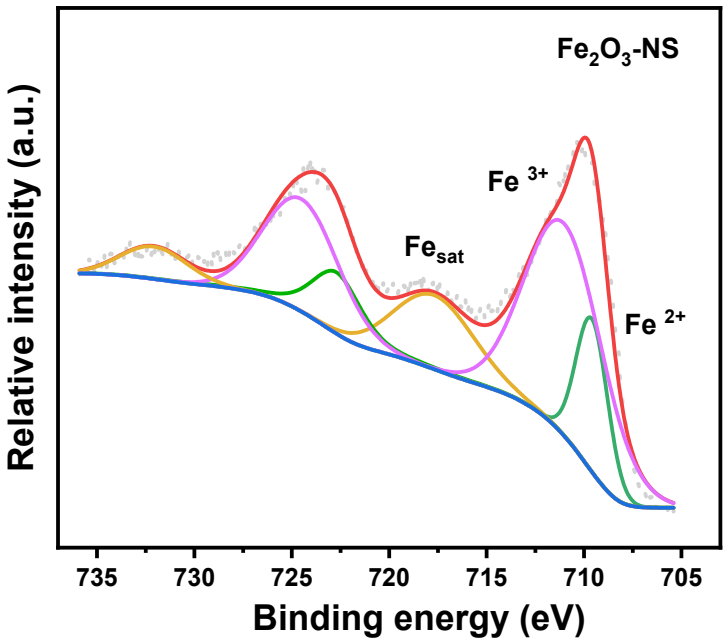

Figure S4. XPS spectra of the Fe_2O_3-NS arrays electrocatalyst for Fe 2p.

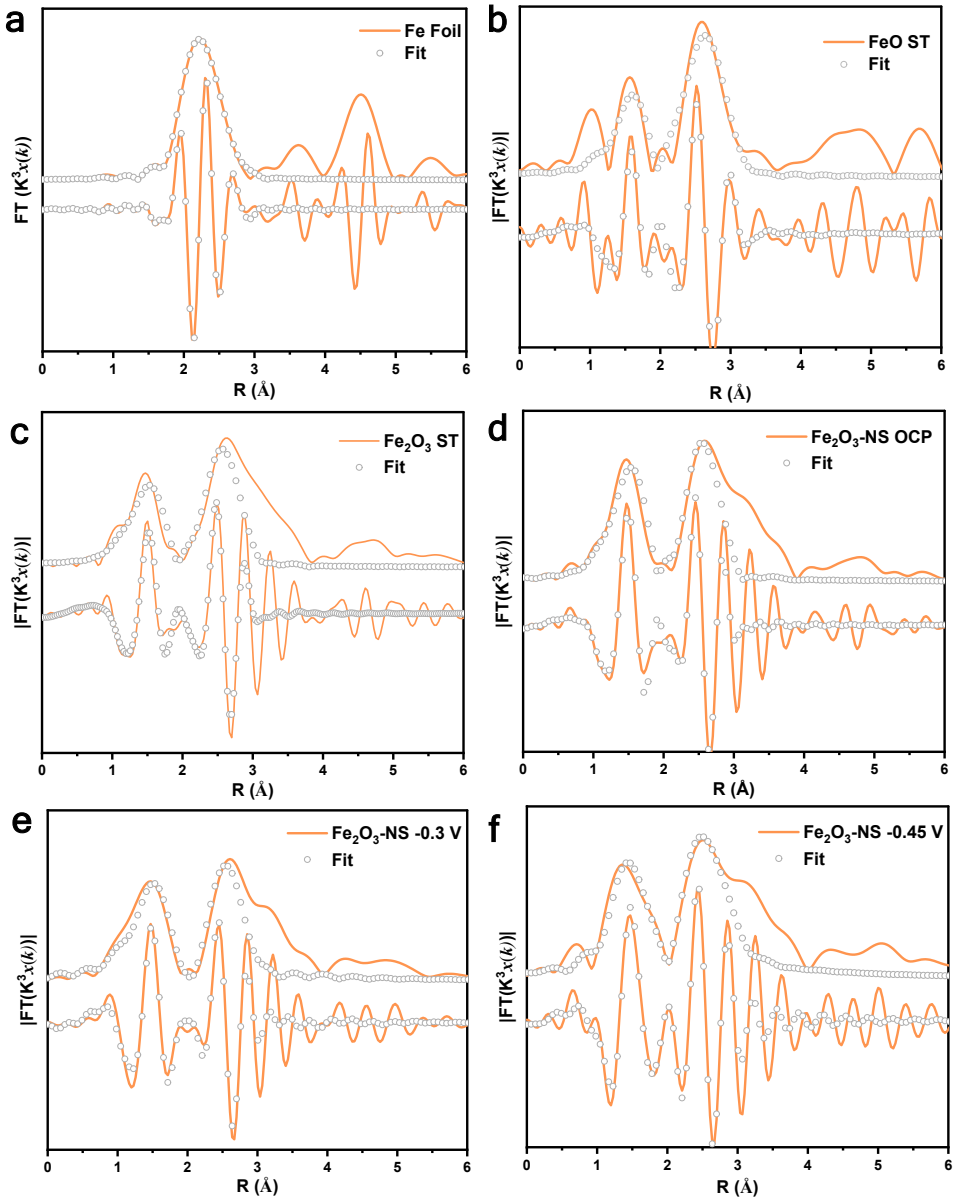

Figure S5. FT-EXAFS fitting spectra for (a) Fe foil, (b) FeO standard sample, (c) Fe_2O_3 standard sample, (d) Fe_2O_3-NS array catalyst, (e) Fe_2O_3-NS -0.3 V and (f) Fe_2O_3-NS -0.45 V in R space.

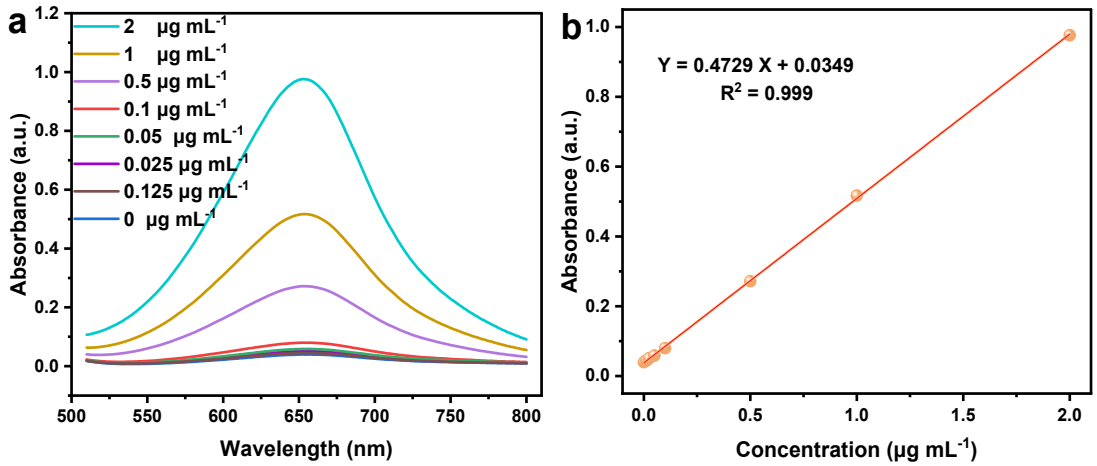

Figure S6. (a) The UV-visible absorption spectra of the standard solutions of NH_4^+, (b) calibration curve used for estimation of NH_3.

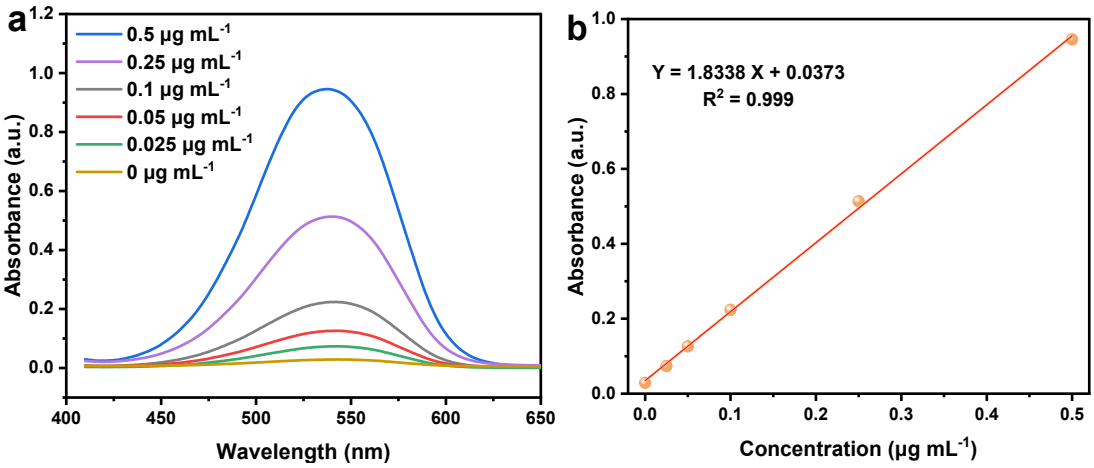

Figure S7. (a) The UV-visible absorption spectra of the standard solutions of NO_2^-, (b) calibration curve used for estimation of NO_2^-.in the solution of 1 M KOH and 0.1 M KNO_3.

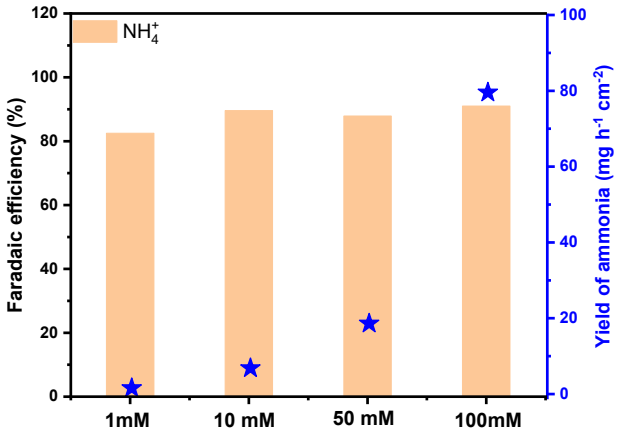

Figure S8. The faradaic efficiency and yield rate of ammonia for Fe_2O_3-NS arrays catalyst tested in the various concentrations of KNO_3.

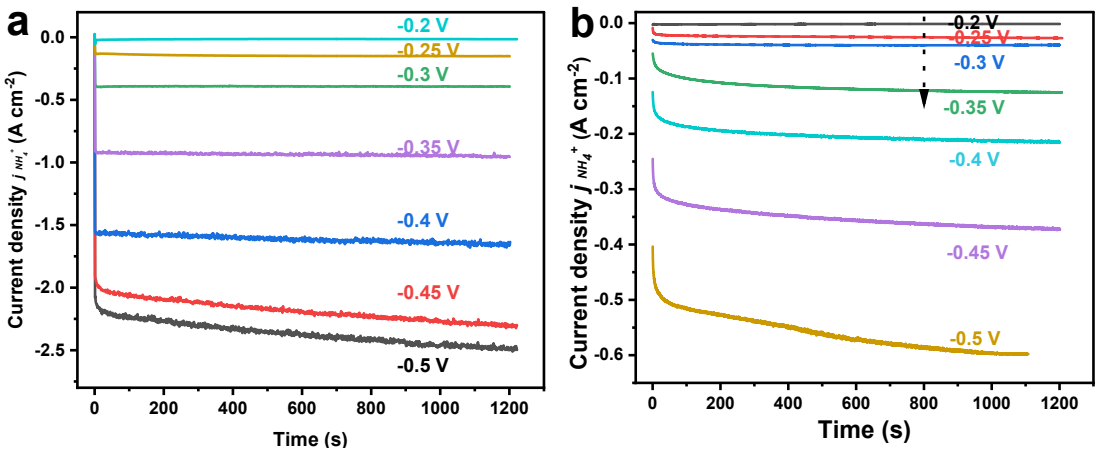

Figure S9. The partial current density of ammonia for (a) Fe_2O_3-NS arrays, and (b) Fe_2O_3-NP catalysts at the given potentials in the mixture solution of 1M KOH and 0.1 M KNO_3.

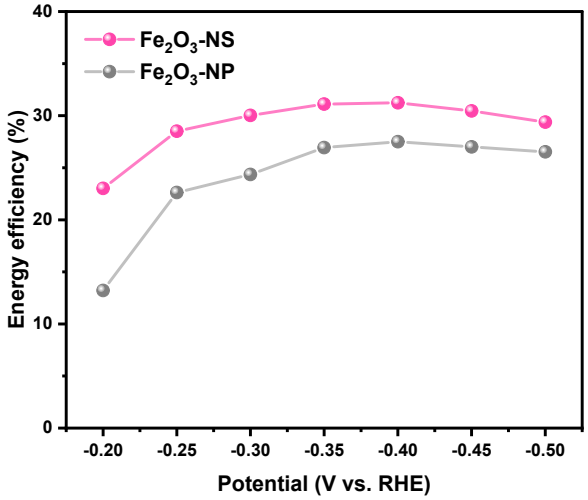

Figure S10. The energy efficiency of Fe_2O_3-NS arrays and Fe_2O_3-NP catalysts under the corresponding potentials.

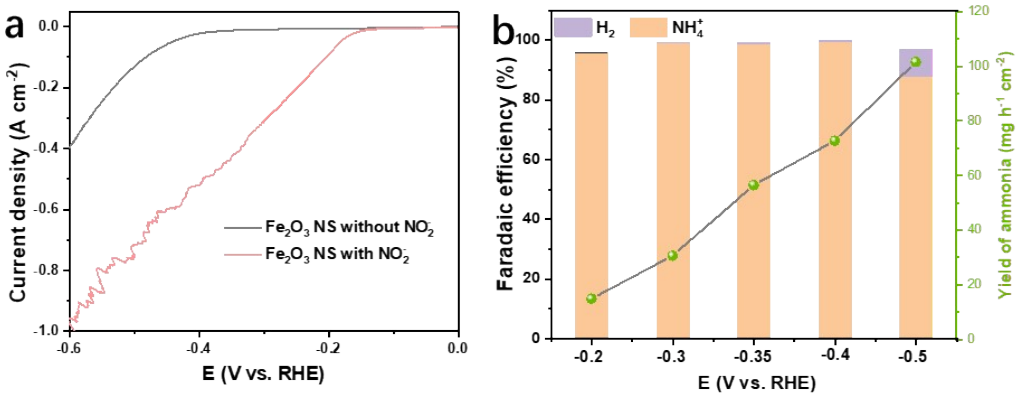

Figure S11. (a) LSV curves of Fe_2O_3 NS in 1M KOH electrolyte and 0.10 M KNO_2/1 M KOH mixed electrolyte, (b) the faradaic efficiency the yield rate of ammonia of Fe_2O_3 NS in the 0.10 M KNO_2/1 M KOH mixed electrolyte.

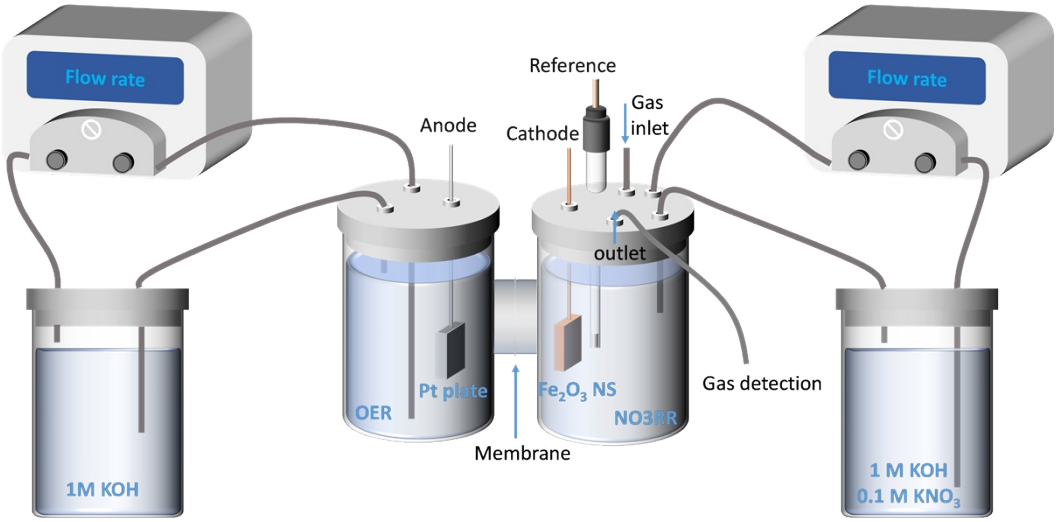

Figure S12. The illustration of home-made continuous flow H-cell for long-term stability of the electrocatalytic reduction of nitrate to ammonia. The flow rates of anode and cathode are 10 mL^{-1}, respectively.

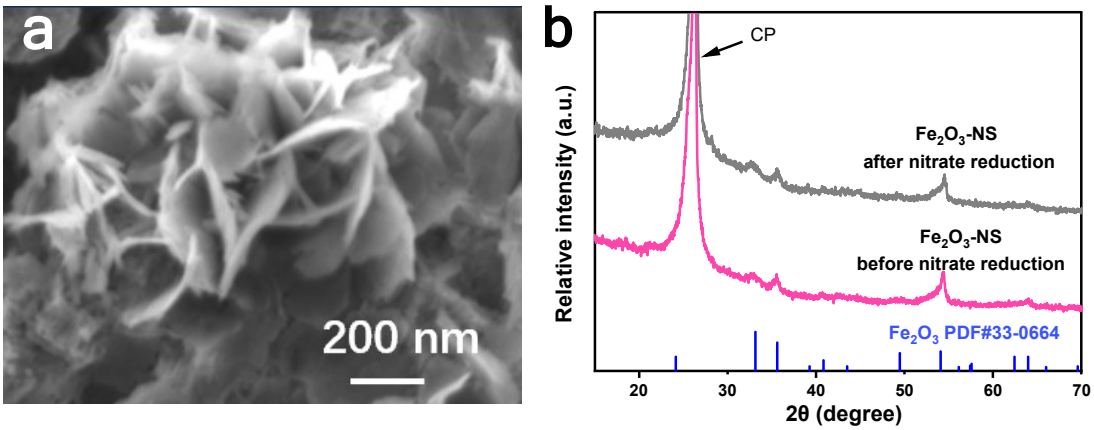

Figure S13. The morphology and structure characterization of Fe_2O_3-NS arrays after the electrocatalytic nitrate reduction. (a) SEM image, (b) XRD patterns.

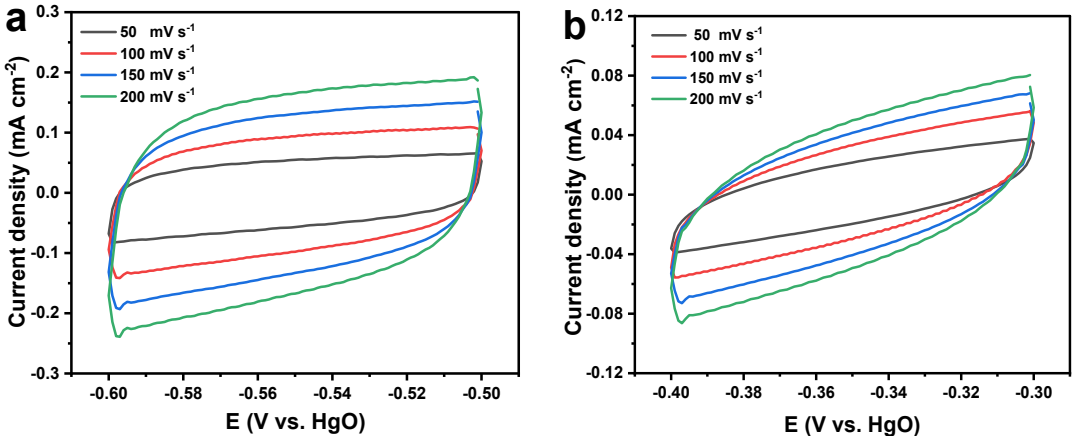

Figure S14. CV curves of (a) Fe_2O_3-NS arrays, (b) Fe_2O_3-NP obtained in the non-Faradaic region with various scan rates from 50 to 200 mV s^{-1}.

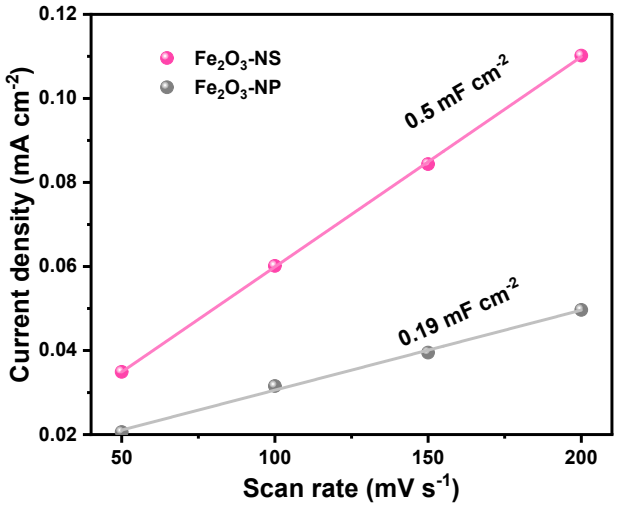

Figure S15. (a) Double-layer capacitance (C_{dl}) of Fe_2O_3-NS arrays and Fe_2O_3-NP catalysts.

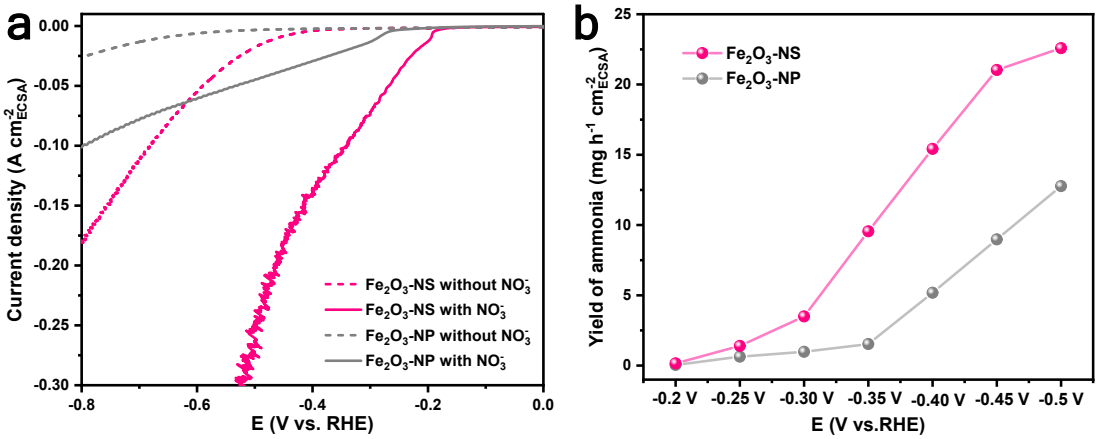

Figure S16. (a) The LSV curves and (b) the yield rate of ammonia normalized to the electrochemical active surface area (EASA) for the Fe_2O_3-NS arrays and Fe_2O_3-NP catalysts.

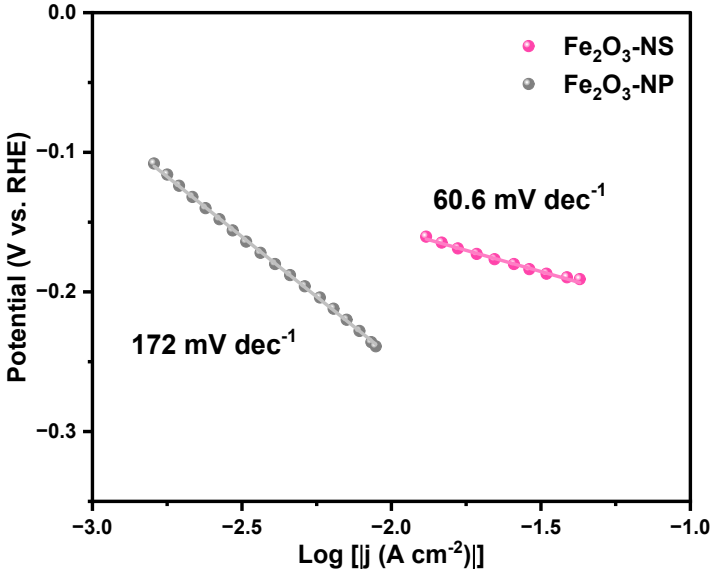

Figure S17. Tafel plots of Fe_2O_3-NS arrays and Fe_2O_3-NP catalysts.

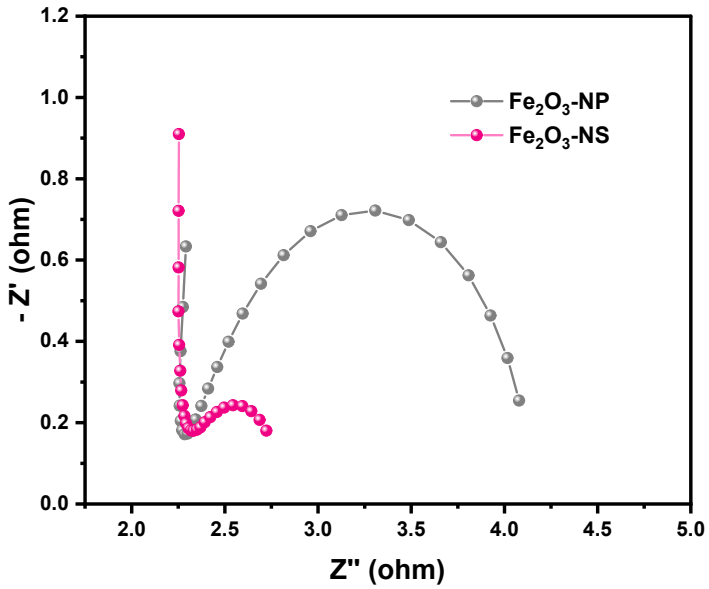

Figure S18. Electrochemical impedance spectroscopy (EIS) of the Fe_2O_3-NS and Fe_2O_3-NP under the applied potential of -0.35 V vs. RHE

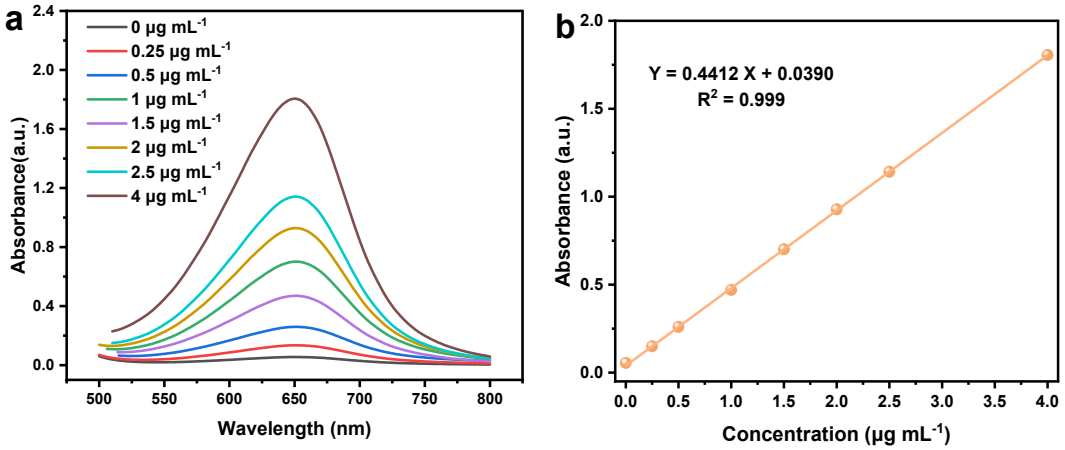

Figure S19. (a) The UV-visible absorption spectra of the standard solutions of NH_4^+ in the solution containing of KOH and KNO_2, (b) calibration curve used for estimation of NH_3 by NH_4^+ ions of different concentrations.

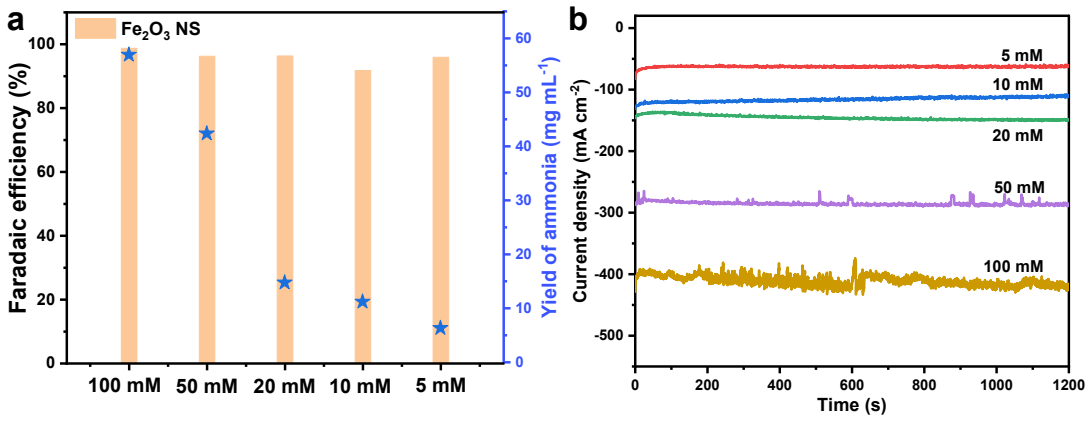

Figure S20. (a) The faradaic efficiency and the yield rate of ammonia for Fe_2O_3-NS sample at the various concentrations of KNO_2, (b) the total current density of ammonia for Fe_2O_3-NS at various concentrations of KNO_2.

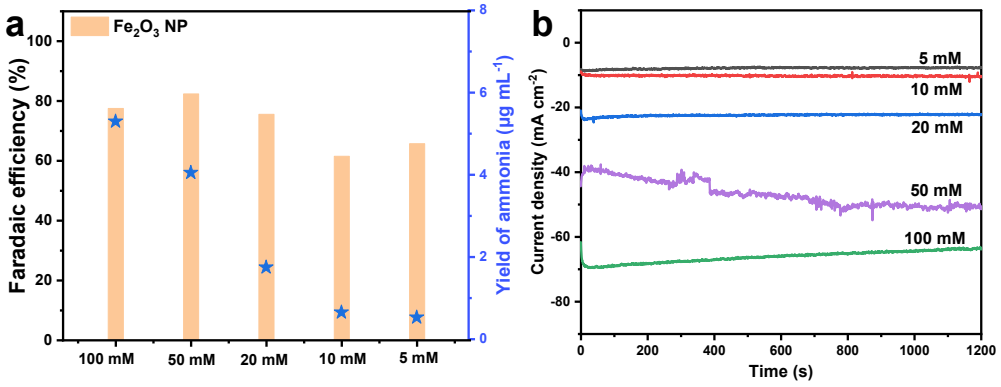

Figure S21. (a) The faradaic efficiency and the yield rate of ammonia for Fe_2O_3-NP sample at the various concentrations of KNO_2, (b) the total current density of ammonia for Fe_2O_3-NP at various concentrations of KNO_2.

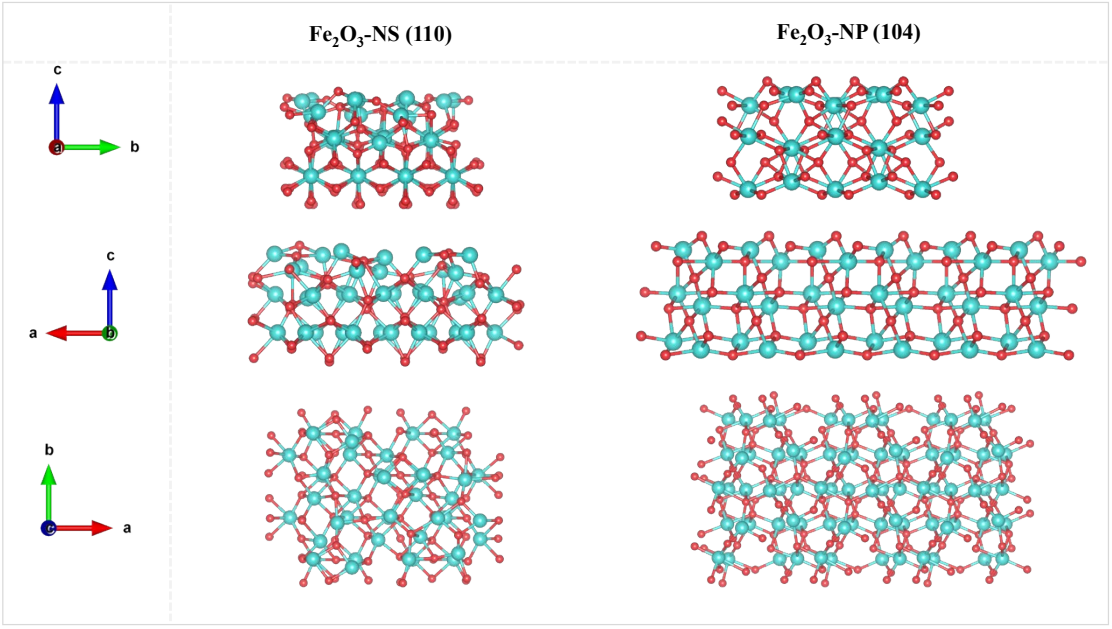

Figure S22. The crystallographic mode of Fe_2O_3-NS (110) and Fe_2O_3-NP (104) view from different axial directions.

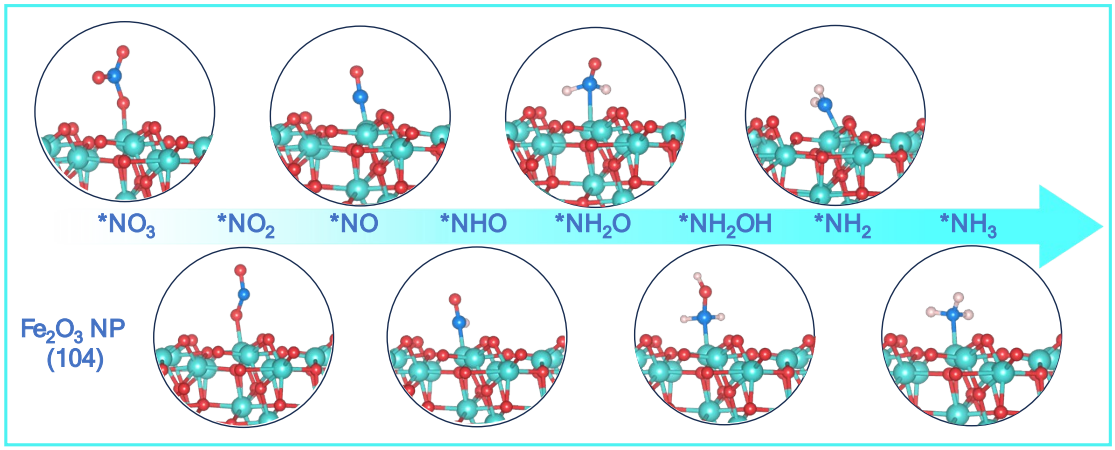

Figure S23. The simplified structures of various NO_3^- reduction reaction intermediates on Fe_2O_3-NP (104) electrocatalyst.

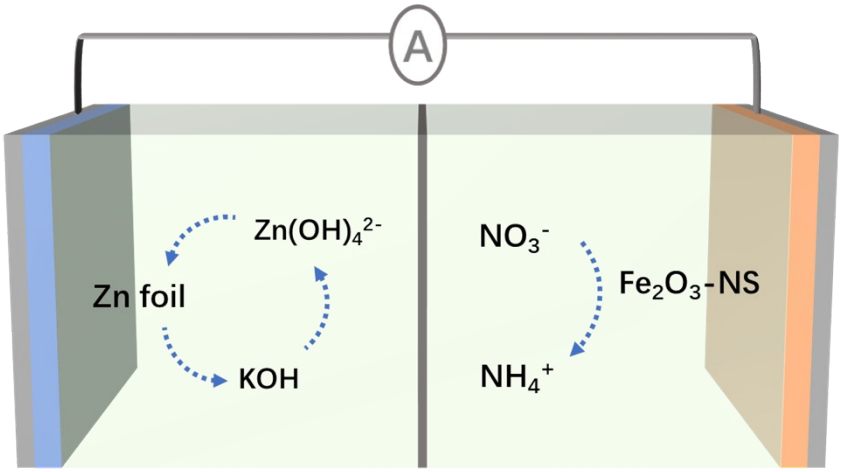

Figure S24. Schematic illustration of a Zn-nitrate battery.

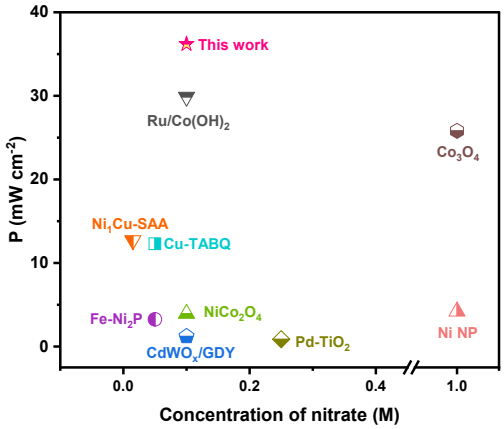

Figure S25. The comparison of Zn-nitrate battery performance using the Fe_2O_3-NS catalyst or other reported catalysts as cathodes.

Table S1. Fitting parameters of Fe K-edge EXAFS curves for different samples.

Samples	Path	N	R	σ^2	ΔE	R(factor)
Fe-foil	Fe-O	6	2.4676	0.0053	5.132	0.0039
	Fe-Fe	6	2.8448	0.0080	5.132	
FeO-ST	Fe-O	1	2.0882	0.0074	1.974	0.0353
	Fe-Fe	1	3.06614	0.0204	1.974	
Fe_2O_3-ST	Fe-O	1	2.98563	0.0116	1.318	0.0242
	Fe-Fe	1	2.01539	0.0115	1.318	
Fe_2O_3-NS-OCP	Fe-O	1	2.0000	0.0096	2.847	0.0197
	Fe-Fe	1	2.9611	0.0095	2.847	
Fe_2O_3-NS-0.3 V	Fe-O	1	1.9916	0.0119	1.744	0.0146
	Fe-Fe	1	2.9477	0.0087	1.744	
Fe_2O_3-NS-0.45 V	Fe-O	1	1.9993	0.0122	1.855	0.0151
	Fe-Fe	1	2.9459	0.0057	1.855	

N, coordination number; R, distance between absorber and backscatter atoms; σ^2, DebyeWaller factor to account for both thermal and structural disorders; ΔE_0, inner potential correction; R factor (%) indicates the goodness of the fit. S_0^2 was fixed to 0.97 as determined from Fe foil fitting.

Table S2. The essential parameters of ammonia synthesis of Fe_2O_3-NS compared with other catalysts.

Catalysts	electrolytes	Yield rate of NH_3 ($mg\ cm^{-2}\ h^{-1}$)	FE %	EE %	Ref.
Fe_2O_3-NS	1 M KOH 0.1 M KNO_3	128.41 175.19 188.17	94.3 95 94.1	31.24 30.54 29.38	This work
Fe_2O_3	0.5 M Na_2SO_4 0.1 M $NaNO_3$	5.576	69.76	17.69	[1]
Fe_2O_3/Fe-N-C	1 M KOH 0.16 M KNO_3	153	100	22.2	[2]
Fe_3O_4	1 M KOH 0.1 M KNO_3	9.5	90	28.09	[3]
$A^5Fe_2O_4$	1 M KOH 0.1 M KNO_3	27.3	98.1	30.6	[4]
Fe SACs	0.10M K_2SO_4 0.50M KNO_3	5.25	75	21.43	[5]
Fe-PPY SACs	0.1 M KOH 0.1 M KNO_3	2.01	100	29.51	[6]
Fe-Cyano	1 M KOH 10 mM KNO_3	42.1	90	28.09	[7]
Cu-Fe_2O_3	0.1 M KOH 0.1 M KNO_3	7.186	100	29.51	[8]
Co-Fe@Fe_2O_3	0.1M Na_2SO_4 500 ppm $NaNO_3$	0.88	85.2	23.24	[9]
Fe-NiP	0.2 M K_2SO_4 50 mM KNO_3	4	93	30.81	[10]
Bi-FeS_2	1 M KOH 0.1 M $NaNO_3$	21.9	98.5	27.56	[11]

RuFe-FeNC	0.5 M Na_2SO_4 0.1 M $NaNO_3$	11.88	92.1	18.91	[12]
Fe-Cu HNG	0.10 M KNO_3, 1.0 M KOH	4.41	92.5	32.64	[13]
FePc	0.1 M K_2SO_4 0.5 M KNO_3	35.07	100	19.78	[14]
Mo_2CT_x:Fe	0.5 M Na_2SO_4 0.1 M $NaNO_3$	0.043	70	20.65	[15]

Table S3. Calculated reaction energy of elementary reactions involved in NO_3RR on Fe_2O_3-NS (110).

Fe_2O_3-NS(110)	**E eV**	**ZPE**	**T/K**	**G eV**
Cat. * NO_3^-	-465.61715	-23.04344	298	-519.28309
***NO_3**	-492.89230	0.31851	298	-523.19629
***NO_2**	-487.27767	0.23578	298	-525.08039
***NO**	-480.51958	0.15584	298	-525.81824
***NHO**	-484.77835	0.48295	298	-526.34740
***NH_2O**	-488.92201	0.80072	298	-526.77079
***NH_2OH**	-495.07885	0.99947	298	-529.32638
***NH_2**	-483.34959	0.69407	298	-528.72102
***NH_3**	-487.28832	0.95795	298	-528.99337

Table S4. Calculated reaction energy of elementary reactions involved in NO_3RR on Fe_2O_3-NP (104).

Fe_2O_3-NP (104)	**E eV**	**ZPE**	**T K**	**G eV**
Cat. * NO_3^-	-999.50971	-23.04344	298	-2.11803
***NO_3**	-1024.93720	0.26602	298	-1.78775
***NO_2**	-1019.18830	0.14537	298	-2.44522
***NO**	-1014.21440	0.14225	298	-0.06481
***NHO**	-1017.98380	0.44434	298	-1.85167
***NH_2O**	-1023.58480	0.79117	298	0.78177
***NH_2OH**	-1026.47660	1.06224	298	-1.05995
***NH_2**	-1016.32440	0.66859	298	-1.71275
***NH_3**	-1021.78580	1.01474	298	1.51512

Reference

[1] T. Li, C. Tang, H. Guo, H. Wu, C. Duan, H. Wang, F. Zhang, Y. Cao, G. Yang, Y. Zhou, *ACS Appl. Mater. Interfaces* **2022**, *14*, 49765-49773.

[2] E. Murphy, B. Sun, M. Rüscher, Y. Liu, W. Zang, S. Guo, Y. H. Chen, U. Hejral, Y. Huang, A. Ly, I. V. Zenyuk, X. Pan, J. Timoshenko, B. R. Cuenya, E. D. Spoerke, P. Atanassov, *Adv. Mater.* **2024**, 2401133.

[3] X. Fan, L. Xie, J. Liang, Y. Ren, L. Zhang, L. Yue, T. Li, Y. Luo, N. Li, B. Tang, Y. Liu, S. Gao, A. A. Alshehri, Q. Liu, Q. Kong, X. Sun, *Nano Research* **2021**, *15*, 3050-3055.

[4] S. Qi, Z. Lei, Q. Huo, J. Zhao, T. Huang, N. Meng, J. Liao, J. Yi, C. Shang, X. Zhang, H. Yang, Q. Hu, C. He, *Adv. Mater.* **2024**, 2403958.

[5] Z.-Y. Wu, M. Karamad, X. Yong, Q. Huang, D. A. Cullen, P. Zhu, C. Xia, Q. Xiao, M. Shakouri, F.-Y. Chen, J. Y. Kim, Y. Xia, K. Heck, Y. Hu, M. S. Wong, Q. Li, I. Gates, S. Siahrostami, H. Wang, *Nat. Commun.* **2021**, *12*, 2870.

[6] P. Li, Z. Jin, Z. Fang, G. Yu, *Energy Environ. Sci.* **2021**, *14*, 3522-3531.

[7] Z. Fang, Z. Jin, S. Tang, P. Li, P. Wu, G. Yu, *ACS Nano* **2021**, *16*, 1072-1081.

[8] J. Wang, Y. Wang, C. Cai, Y. Liu, D. Wu, M. Wang, M. Li, X. Wei, M. Shao, M. Gu, *Nano Lett.* **2023**, *23*, 1897-1903.

[9] S. Zhang, M. Li, J. Li, Q. Song, X. Liu, *Proc Natl Acad Sci USA* **2022**, *119*, 2115504119.

[10] R. Zhang, Y. Guo, S. Zhang, D. Chen, Y. Zhao, Z. Huang, L. Ma, P. Li, Q. Yang, G. Liang, C. Zhi, *Adv. Energy Mater.* **2022**, *12*, 2103872.

[11] G. Zhang, G. Wang, Y. Wan, X. Liu, K. Chu, *ACS Nano* **2023**, *17*, 21328-21336.

[12] X. Zhao, Y. Jiang, M. Wang, S. Liu, Z. Wang, T. Qian, C. Yan, *Adv. Energy Mater.* **2023**, *13*, 2301409.

[13] S. Zhang, J. Wu, M. Zheng, X. Jin, Z. Shen, Z. Li, Y. Wang, Q. Wang, X. Wang, H. Wei, J. Zhang, P. Wang, S. Zhang, L. Yu, L. Dong, Q. Zhu, H. Zhang, J. Lu, *Nat. Commun.* **2023**, *14*, 3634.

[14] S. Sarkar, A. Adalder, S. Paul, S. Kapse, R. Thapa, U. K. Ghorai, *Appl. Catal. B: Environ.* **2024**, *343*, 123580.

[15] D. F. Abbott, Y. Z. Xu, D. A. Kuznetsov, P. Kumar, C. R. Müller, A. Fedorov, V. Mougel, *Angew. Chem. Int. Ed.* **2023**, *62*, e202313746